



## **Monodispersed FeS<sub>2</sub> Electrocatalyst Anchored to Nitrogen-Doped Carbon Host for Lithium–Sulfur Batteries**

Downloaded from: <https://research.chalmers.se>, 2025-12-04 23:22 UTC

Citation for the original published paper (version of record):

Sun, W., Liu, S., Li, Y. et al (2022). Monodispersed FeS<sub>2</sub> Electrocatalyst Anchored to Nitrogen-Doped Carbon Host for Lithium–Sulfur Batteries. *Advanced Functional Materials*, 32(43).  
<http://dx.doi.org/10.1002/adfm.202205471>

N.B. When citing this work, cite the original published paper.

# Monodispersed FeS<sub>2</sub> Electrocatalyst Anchored to Nitrogen-Doped Carbon Host for Lithium–Sulfur Batteries

Weiwei Sun,\* Shuangke Liu, Yujie Li, Danqin Wang, Qingpeng Guo, Xiaobin Hong, Kai Xie, Zhongyun Ma, Chunman Zheng,\* and Shizhao Xiong\*

Despite their high theoretical energy density, lithium–sulfur (Li–S) batteries are hindered by practical challenges including sluggish conversion kinetics and shuttle effect of polysulfides. Here, a nitrogen-doped continuous porous carbon (CPC) host anchoring monodispersed sub-10 nm FeS<sub>2</sub> nanoclusters (CPC@FeS<sub>2</sub>) is reported as an efficient catalytic matrix for sulfur cathode. This host shows strong adsorption of polysulfides, promising the inhibition of polysulfide shuttle and the promoted initial stage of catalytic conversion process. Moreover, fast lithium ion (Li-ion) diffusion and accelerated solid–solid conversion kinetics of Li<sub>2</sub>S<sub>2</sub> to Li<sub>2</sub>S on CPC@FeS<sub>2</sub> host guarantee boosted electrochemical kinetics for conversion process of sulfur species in Li–S cell, which gives a high utilization of sulfur under practical conditions of high loading and low electrolyte/sulfur (E/S) ratio. Therefore, the sulfur cathode (S/CPC@FeS<sub>2</sub>) delivers a high specific capacity of 1459 mAh g<sup>−1</sup> at 0.1 C, a stable cycling over 900 cycles with ultralow fading rate of 0.043% per cycle, and an enhanced rate capability compared with cathode only using carbon host. Further demonstration of this cathode in Li–S pouch cell shows a practical energy density of 372 Wh kg<sup>−1</sup> with a sulfur loading of 7.1 mg cm<sup>−2</sup> and an E/S ratio of 4 μL mg<sup>−1</sup>.

electric vehicles and portable electronics devices.<sup>[1–4]</sup> Lithium–sulfur (Li–S) batteries are considered as one of the most promising candidates among next-generation battery technologies due to their low cost, high theoretical specific capacity (1675 mAh g<sup>−1</sup>), and energy density (2600 Wh kg<sup>−1</sup>).<sup>[5–7]</sup> Despite of these advantages, Li–S batteries are yet to achieve the sufficient properties for commercialization because of low utilization of active material and limited long-term cycling ability, which are primarily attributed to the poor conductivity of elemental sulfur/lithium sulfides, shuttle effect of lithium polysulfides (LiPSs), and sluggish kinetics for the conversion of sulfur species.<sup>[8–11]</sup>

To address these issues, tremendous effort has been devoted to the fabrication of effective hosts for sulfur cathode. Conductive carbon-based matrixes with high specific surface area and porosity are

widely studied as host materials, which can provide accommodation for active mass sulfur, buffering space for the volume change, and efficient network for electron transfer in electrodes.<sup>[12–14]</sup> Despite great progress achieved, nonpolar carbonaceous host materials possess poor chemical affinity to polar LiPSs, resulting in the active diffusion of LiPSs away from cathode since they are highly soluble in the ether-based liquid electrolyte. To suppress the shuttle effect that is based on the diffusion of LiPSs, polar transition metal materials such as oxides,<sup>[15,16]</sup> chalcogenides,<sup>[17–20]</sup> nitrides,<sup>[21,22]</sup> phosphides,<sup>[23,24]</sup> and carbides<sup>[25,26]</sup> have been introduced into carbon host and they are demonstrated to present strong chemical interactions toward LiPSs. However, the limited adsorption sites of the carbon host will be easily occupied to reach a saturated state due to the sluggish conversion kinetics, leading to the constant diffusion of LiPSs into electrolyte, especially for the sulfur cathodes with high loading active mass.<sup>[27–29]</sup> During the discharge process of Li–S battery, the rate-determining step for the conversion of sulfur species is the solid–solid conversion process from Li<sub>2</sub>S<sub>2</sub> to Li<sub>2</sub>S which contributes almost half theoretical capacity and the high activation energy of this process restricts the full conversion, leading to low utilization of sulfur as well as limited capacity obtained.<sup>[30–32]</sup> Therefore, design of electrocatalyst for accelerating the reaction kinetics of sulfur is a promising strategy for developing high-energy-density Li–S batteries.


## 1. Introduction

Increasing demand for advanced energy storage technologies has been created owing to the rapid development of

W. Sun, S. Liu, Y. Li, D. Wang, Q. Guo, X. Hong, K. Xie, C. Zheng  
College of Aerospace Science and Engineering  
National University of Defense Technology  
Changsha 410073, China  
E-mail: wwsun@nudt.edu.cn; zhengchunman@nudt.edu.cn

Z. Ma  
Department of Chemistry  
Key Laboratory of Environmentally Friendly Chemistry and Applications  
of Ministry of Education  
Xiangtan University  
Xiangtan 411105, China

S. Xiong  
Department of Physics  
Chalmers University of Technology  
Göteborg SE 412 96, Sweden  
E-mail: shizhao.xiong@chalmers.se

 The ORCID identification number(s) for the author(s) of this article can be found under <https://doi.org/10.1002/adfm.202205471>.

© 2022 The Authors. Advanced Functional Materials published by Wiley-VCH GmbH. This is an open access article under the terms of the Creative Commons Attribution License, which permits use, distribution and reproduction in any medium, provided the original work is properly cited.

DOI: 10.1002/adfm.202205471

Recently, iron (Fe)-based chalcogenides have been demonstrated to present efficient catalytic effect for hydrogen evolution reaction, water splitting, and oxygen reduction reaction, showing advantages of high conductivity, good economy, and chemical stability.<sup>[33,34]</sup> For application in Li-S batteries, Fe-based sulfides have been employed as electrocatalyst for the conversion of sulfur species.<sup>[35,36]</sup> However, the energy density and cycling life of the Li-S batteries are still hindered by the low surface area, low porosity, and poor microstructure of the electrocatalysts. Therefore, design and fabrication of Fe-based sulfides as efficient electrocatalyst of sulfur species is the key for improving the utilization of sulfur in high-energy-density Li-S batteries. To build practical Li-S batteries, pouch cell is the important prototype to evaluate the key performance of Li-S cells including energy density and areal capacity under the realistic conditions for commercialization, like high loading of sulfur ( $>5 \text{ mg cm}^{-2}$ ), low ratio of electrolyte/sulfur (E/S) ( $<5 \text{ mL mg}^{-1}$ ), and limited excess Li anode.<sup>[37–39]</sup> Nevertheless, electrocatalysts like Fe-based sulfides are barely reported in Li-S pouch cells under practical condition since the large-scale synthesis of these catalysts is still challenging.

In this work, we report a cost-effective nitrogen-doped continuous porous carbon (CPC) host anchoring sub-10 nm  $\text{FeS}_2$  nanoclusters as an efficient electrocatalyst ( $\text{CPC@FeS}_2$ ), which is aiming to accelerate the conversion kinetics of  $\text{Li}_2\text{S}_2$  to  $\text{Li}_2\text{S}$  for high energy density Li-S batteries. Our results show that the synergistic engineering of  $\text{CPC@FeS}_2$  host delivers large interior space for high loading of sulfur and the dramatic volume change during conversion process of sulfur species. Moreover, the host provides abundant catalytic active sites for adsorption of polysulfides and conversion of the solid intermediate products like  $\text{Li}_2\text{S}_2$ . Therefore, the sluggish kinetic for solid-solid

conversion of  $\text{Li}_2\text{S}_2$  to  $\text{Li}_2\text{S}$  is significantly promoted, contributing to the suppression of shuttle effect and high utilization of active mass. The sulfur cathode based on the host ( $\text{S/CPC@FeS}_2$ ) presents a high specific capacity, improved rate capability and long-term cycling stability with 0.043% capacity fading rate per cycle for 900 cycles. Li-S pouch cell with this cathode shows a competitive energy density of  $338 \text{ Wh kg}^{-1}$  under conditions of high areal capacity of  $8.5 \text{ mAh cm}^{-2}$ , high sulfur loading of  $8.4 \text{ mg cm}^{-2}$ , and a very low E/S ratio of  $3.5 \text{ mL mg}^{-1}$ . Furthermore, optimization of sulfur loading and E/S ratio can lift the energy density of Li-S pouch cell to a record high level as  $372 \text{ Wh kg}^{-1}$ . Our results shed light on the design of advanced carbon host possessing efficient electrocatalysts and conductive network for high performance sulfur cathode as well as practical Li-S battery.

## 2. Results and Discussion

The synthesis procedure of  $\text{S/CPC@FeS}_2$  composite is illustrated in **Figure 1a**. The nitrogen-doped CPC host was first synthesized through a carbonization process followed by acid etching, where sodium citrate was employed as self-template as well as carbon precursor and melamine was used as source of nitrogen functional group.<sup>[40]</sup> The nitrogen group on the surface of the CPC host endows the electronegative property and the adsorption energy ( $E_{\text{ads}}$ ) for  $\text{Fe}^{3+}$  with N atom is  $-4.87 \text{ eV}$ , which is much higher than that with C atom ( $-2.61 \text{ eV}$ ), as seen in **Figure 1b**. Consequently, the  $\text{Fe}^{3+}$  ions highly prefer to adsorb on the nitrogen-doped active site of CPC when it is dispersed in  $\text{FeCl}_3$  aqueous solution. A further sulfidation step uniformly creates sub-10 nm  $\text{FeS}_2$  nanoclusters on the CPC host, named

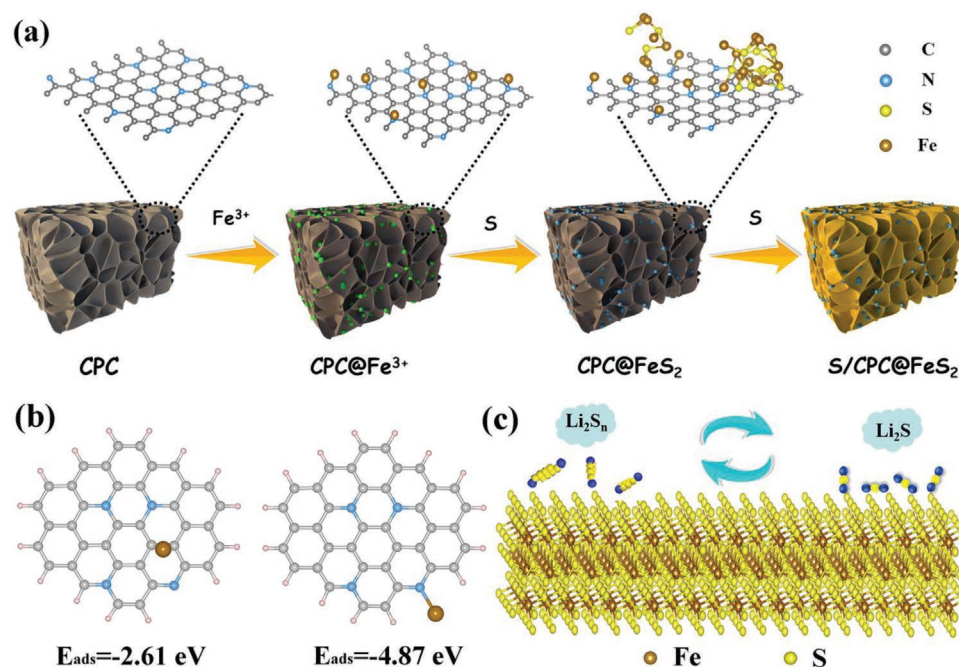


**Figure 1.** Schematic illustration of synthesis of cathode host and the electrocatalytic process. a) Synthesis process of  $\text{S/CPC@FeS}_2$  composite. b) Optimized adsorption configurations and the corresponding binding energy of  $\text{Fe}^{3+}$  with C atom and N atom, respectively. c) Electrocatalytic sites of  $\text{FeS}_2$  for sulfur species.



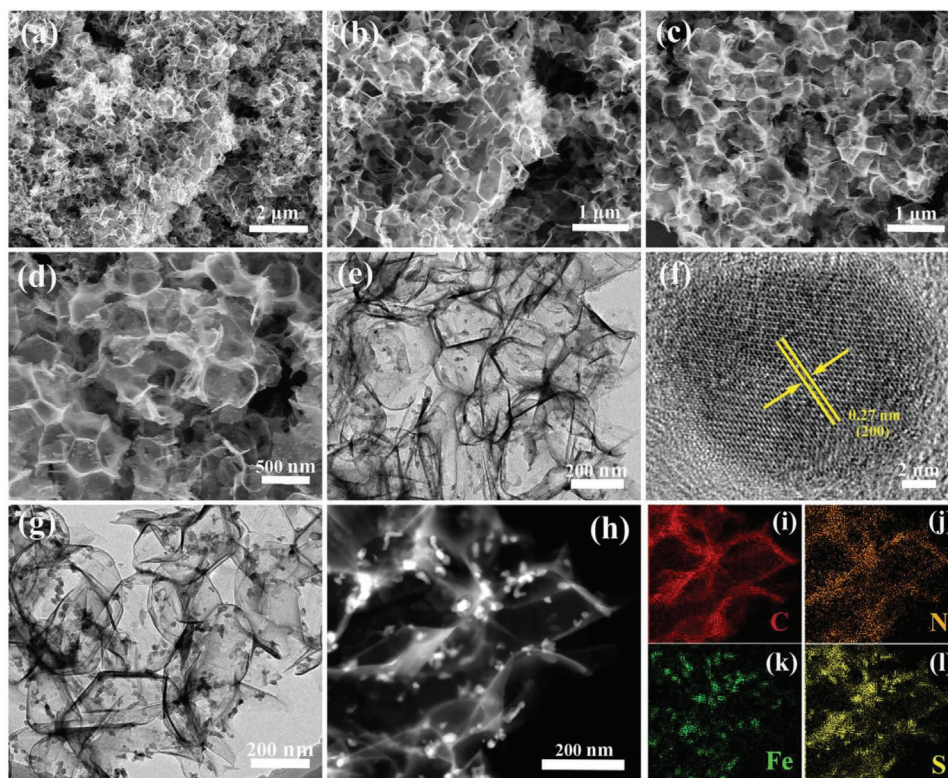


**Figure 2.** Morphology of CPC@FeS<sub>2</sub> host and sulfur cathode. SEM images of a,b) CPC and c,d) CPC@FeS<sub>2</sub>. e,f) High-resolution transmission electron microscopy (HRTEM) images of CPC@FeS<sub>2</sub> host. g–l) TEM images and the corresponding EDS elemental distribution maps of S/CPC@FeS<sub>2</sub> cathode.

as CPC@FeS<sub>2</sub>. The FeS<sub>2</sub> nanoparticle is expected to show a crystal structure of cubic symmetry (Figure S1, Supporting Information) and the CPC@FeS<sub>2</sub> host is promising to deliver abundant catalytic sites for the conversion of sulfur species (Figure 1c). Lastly, the sulfur cathode based on this carbon host (S/CPC@FeS<sub>2</sub>) was obtained by the melting-diffusion process.

To obtain the microstructures of the CPC@FeS<sub>2</sub> host and as-prepared sulfur cathode, scanning electron microscopy (SEM) and high-resolution transmission electron microscope (TEM) are conducted. SEM images of CPC host (Figure 2a,b) show the nanoarchitecture with continuous porous network constructed by massive carbon nanosheets. This structure is further demonstrated by TEM images in Figure S2a,b of the Supporting Information and the carbon nanosheets presents a thickness of  $\approx 7$  nm. The integrated porous structure fabricated by the ultrathin carbon nanosheets allows the high electronic/ionic conductivity in the network and enough internal space for volume change as well as high loading of active sulfur. The FeS<sub>2</sub> nanoparticles were uniformly anchored to the nitrogen-doped CPC host by electrostatic adsorption of Fe<sup>3+</sup> to nitrogen atoms and the host maintains the nanostructure during the growth process of FeS<sub>2</sub>, as shown in Figure 2c–e. The energy dispersive X-ray spectroscopy (EDS) of CPC@FeS<sub>2</sub> host indicates the coexistence of C, N, Fe, and S elements, as seen in Figure S2e of the Supporting Information. Interestingly, if only sodium citrate is used as carbon precursor without melamine (precursor for nitrogen doping), the SEM images of the final product show that almost no FeS<sub>2</sub> nanoparticle is loaded on the carbon nanosheet (Figure S3, Supporting Information). Moreover, the

typical diffraction peaks of FeS<sub>2</sub> cannot be discerned in X-ray diffraction (XRD) pattern of the product prepared without melamine, see Figure S4 of the Supporting Information. This proves that the monodispersed FeS<sub>2</sub> nanoclusters are enabled by the doping nitrogen atoms. The nanostructure of FeS<sub>2</sub> is further revealed by TEM images in Figure 2f, showing a nanocrystalline with a diameter of  $\approx 5$  nm and an interplanar spacing of 0.27 nm which is corresponding to the (200) crystal planes.<sup>[35]</sup> The sulfur cathode based on the carbon host (S/CPC@FeS<sub>2</sub>) shows similar morphology (Figure 2g; Figure S2c,d, Supporting Information) to that before the infiltration of active mass sulfur, indicating a robust structure of the host. Furthermore, the EDS mapping of S/CPC@FeS<sub>2</sub> cathode (Figure 2h–l) reveals the uniform distribution of C, N, Fe, and S elements in the composite.

To understand the interaction between sulfur and carbon host, chemical and structural analysis of the host and S/CPC@FeS<sub>2</sub> cathode are carried out. The negative zeta potential CPC powder in deionized water (Figure 3a) suggests that the doping nitrogen atoms promise adsorption sites for Fe<sup>3+</sup> and thus homogeneous distribution of formed FeS<sub>2</sub>. X-ray photoelectron spectroscopy (XPS) for CPC host in Figure S5 of the Supporting Information shows the presence of C, N, and O elements. The corresponding high-resolution C 1s spectrum (Figure 3b) is fitted with three peaks at 288.3, 285.5, and 284.4 eV, which are in agreement with C=O, C–N, and C–C, respectively.<sup>[41]</sup> The C–N functional groups show the strong bonding between the doped nitrogen atoms and carbon host. Fitting of N 1s spectrum of CPC (Figure 3c) reveals four nitrogen compounds, pyridinic N at 398.2 eV, pyrrolic N at 400.0 eV, graphitic N at 400.5 eV, and

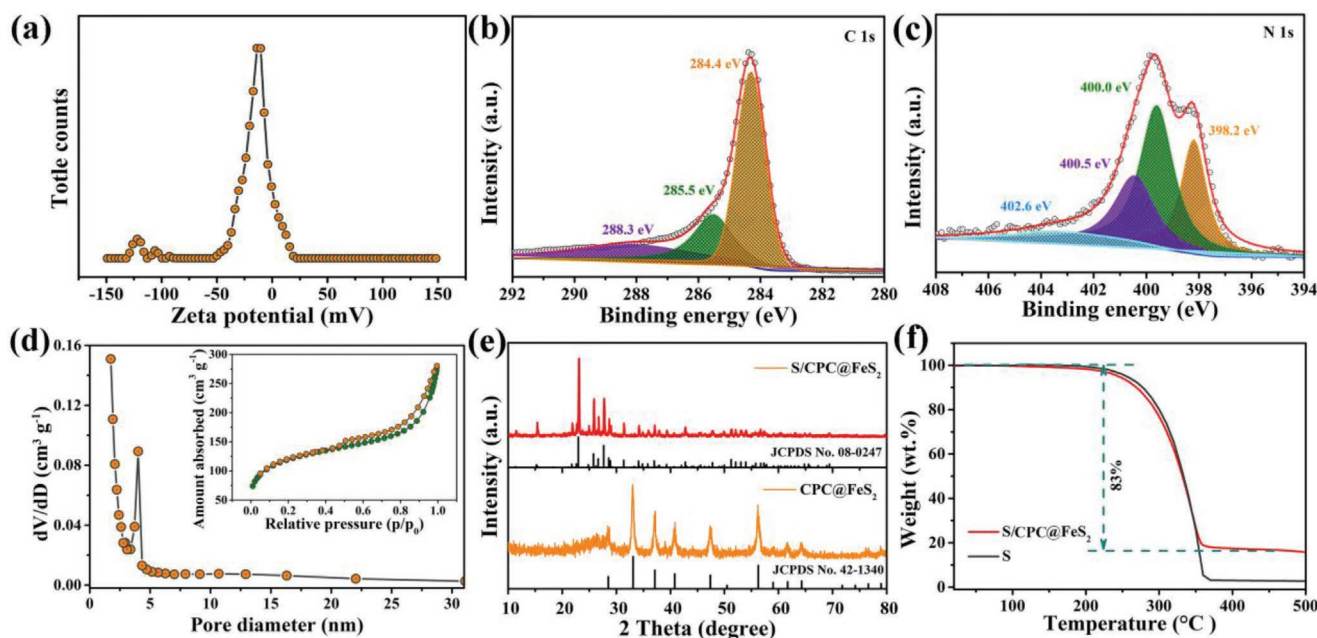


**Figure 3.** Chemical and structural analysis of carbon host and sulfur cathode. a) Zeta potential of CPC powder in deionized water. b,c) High-resolution XPS spectra of C1s and N1s for CPC. d) Pore size distribution and corresponding nitrogen adsorption/desorption isotherms (the inset) of CPC. e) XRD patterns of CPC@FeS<sub>2</sub> host and S/CPC@FeS<sub>2</sub> cathode. f) TGA curves of sulfur and S/CPC@FeS<sub>2</sub> cathode.

oxidic N at 402.6 eV, which allow high electrical conductivity of the host and massive adsorption sites for LiPSs.<sup>[42]</sup> Figure S6 of the Supporting Information shows the Raman spectra of pure CPC and CPC@FeS<sub>2</sub>, which contain main peaks corresponding to vibration modes for graphitic edge defects (D 1350 cm<sup>-1</sup>) and ideal graphite (G 1580 cm<sup>-1</sup>). It can be seen that the  $I_G/I_D$  of CPC is determined as 1.11, slightly lower than that of CPC@FeS<sub>2</sub> composite (1.19), implying a higher graphitization of the obtained CPC@FeS<sub>2</sub>. Abundant mesopores of 4 nm in diameter and high specific surface area of 405 m<sup>2</sup> g<sup>-1</sup> are obtained for the CPC host by Brunauer–Emmett–Teller (BET) method (see Figure 3d), showing the great capacity for sulfur loading, volume change, and abundant catalytic sites on the host surface. After infiltrated with sulfur, the specific surface area of the S/CPC@FeS<sub>2</sub> is measured to be 10 m<sup>2</sup> g<sup>-1</sup> (Figure S7, Supporting Information). The characteristic peaks in XRD patterns (Figure 3e) of CPC@FeS<sub>2</sub> host are attributed to crystalline cubic FeS<sub>2</sub> (JCPDS No. 42–1340).<sup>[43]</sup> Moreover, the typical diffraction peaks of sulfur in the S/CPC@FeS<sub>2</sub> cathode reveal the successful loading of sulfur into the host by the melting-diffusion method. Thermal gravimetric analysis (TGA) was conducted to identify the content of various species in the carbon host as well as in the as-prepared sulfur cathode. The TGA curves in Figure 3f and Figure S8 (Supporting Information) show that the content of FeS<sub>2</sub> in the CPC@FeS<sub>2</sub> host is about 25 wt% and the mass fraction of sulfur in the S/CPC@FeS<sub>2</sub> cathode is 83%.

To corroborate the interaction between the carbon host and LiPSs, which are the intermediate products during the operation of Li–S battery, the adsorption experiments were performed by mixing CPC@FeS<sub>2</sub> or CPC powder into solution of Li<sub>2</sub>S<sub>6</sub>. Optical visualization of the experiments is shown in Figure 4a and the solution with CPC@FeS<sub>2</sub> powder was obviously decolorized after shelving while the one with CPC is still

in dark tawny color, suggesting much more adsorption of LiPSs in CPC@FeS<sub>2</sub> host compared to that with CPC host.<sup>[21]</sup> The CPC@FeS<sub>2</sub> host adsorbed with LiPSs is analyzed by high-resolution XPS and the fitted spectra of Fe 2p are presented in Figure 4b. After the adsorption of LiPSs, the Fe 2p peaks for CPC@FeS<sub>2</sub> host show a shift to lower binding energy, which reveals the chemical affinity between them. Furthermore, a new peak around 720 eV shows up and this is attributed to new FeS<sub>x</sub> species formed by the chemical reaction between FeS<sub>2</sub> and LiPSs, which is an additional proof for the strong interactions of polar FeS<sub>2</sub> with LiPSs.<sup>[41,44]</sup> The effective chemisorption of LiPSs on the CPC@FeS<sub>2</sub> host is further demonstrated by the positive shift of S 2p peaks and the new peak 168 eV (Figure 4c), which is corresponding to the oxidation of sulfur species on the host.<sup>[45]</sup>

The intrinsic interaction between FeS<sub>2</sub> and sulfur species was simulated at atomic level by theoretical density functional theory (DFT) to elaborate the adsorption mechanism.<sup>[46–50]</sup> Figure 4e–g shows the rendering for optimized geometric configurations of typical soluble sulfur species on (200) surface of FeS<sub>2</sub> and the corresponding binding energies ( $E_b$ ) are presented in Figure 4d. The calculated  $E_b$  for Li<sub>2</sub>S<sub>4</sub>, Li<sub>2</sub>S<sub>6</sub>, and Li<sub>2</sub>S<sub>8</sub> are 1.10, 1.36, and 1.73 eV, respectively. The results obtained on the FeS<sub>2</sub> surface are much higher than that on N-doped carbon as previously reported.<sup>[51]</sup> Our simulation results are consistent with the adsorption experiment, demonstrating the strong binding strength of LiPSs to CPC@FeS<sub>2</sub> host. It is generally accepted that the adsorption is the first step for catalytic conversion process and the strong adsorption of sulfur species in CPC@FeS<sub>2</sub> host shows a great promise for the efficiency of FeS<sub>2</sub> electrocatalyst.

Apart from the chemical adsorption, there are other rate controlling steps for the conversion of sulfur species in Li–S



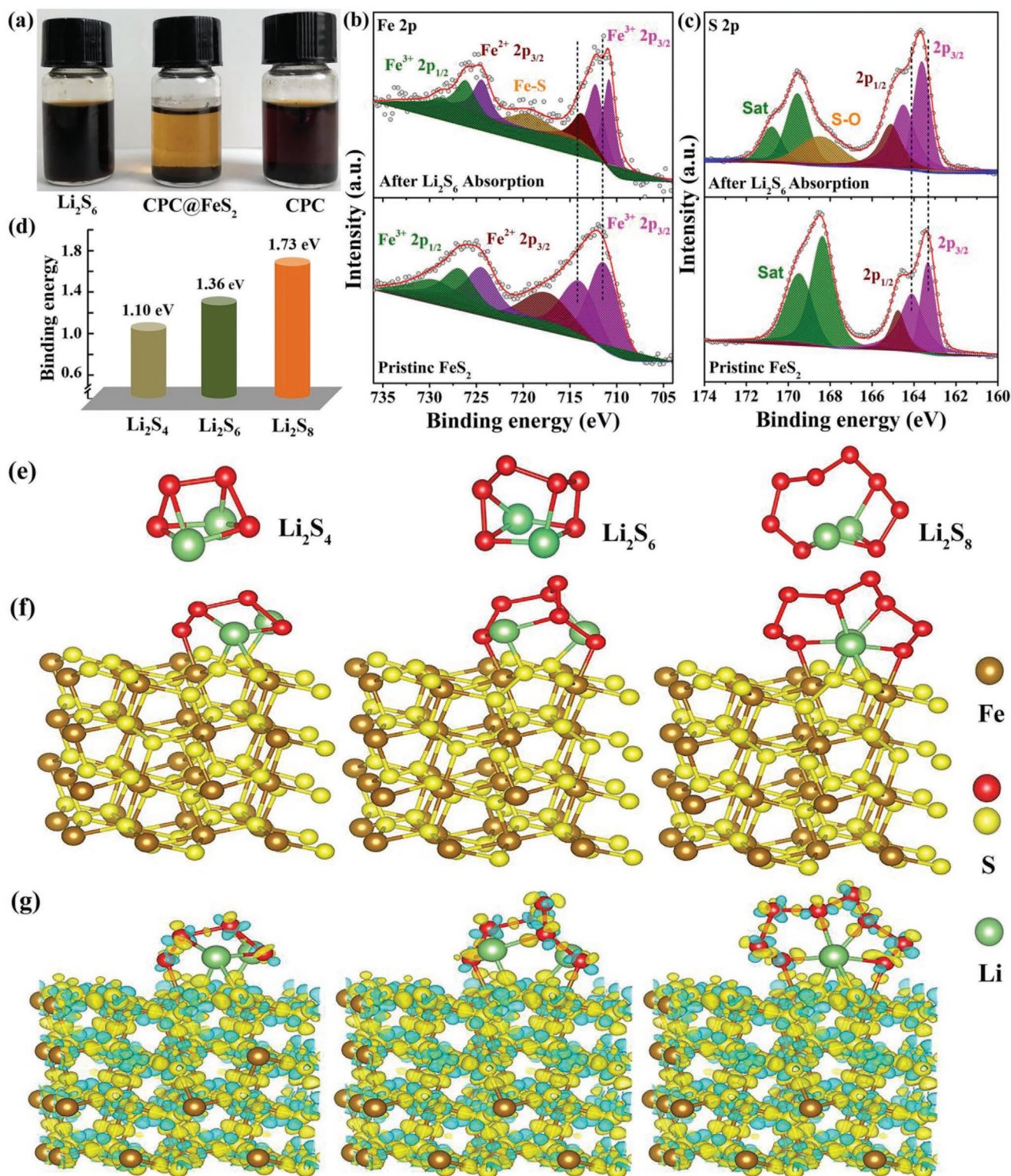


**Figure 4.** Interaction between polysulfides and CPC@FeS<sub>2</sub> host. a) Visualization experiments for the adsorption of polysulfides by CPC host and CPC@FeS<sub>2</sub> host. b,c) High-resolution XPS spectra at Fe 2p (b) and S 2p (c) regions for pristine CPC@FeS<sub>2</sub> and CPC@FeS<sub>2</sub>-Li<sub>2</sub>S<sub>6</sub>, respectively. d) Simulation of binding energy and e-g) optimized adsorption configurations and electronic density differences for Li<sub>2</sub>S<sub>4</sub>, Li<sub>2</sub>S<sub>6</sub>, and Li<sub>2</sub>S<sub>8</sub> on FeS<sub>2</sub> (200) surface, respectively.

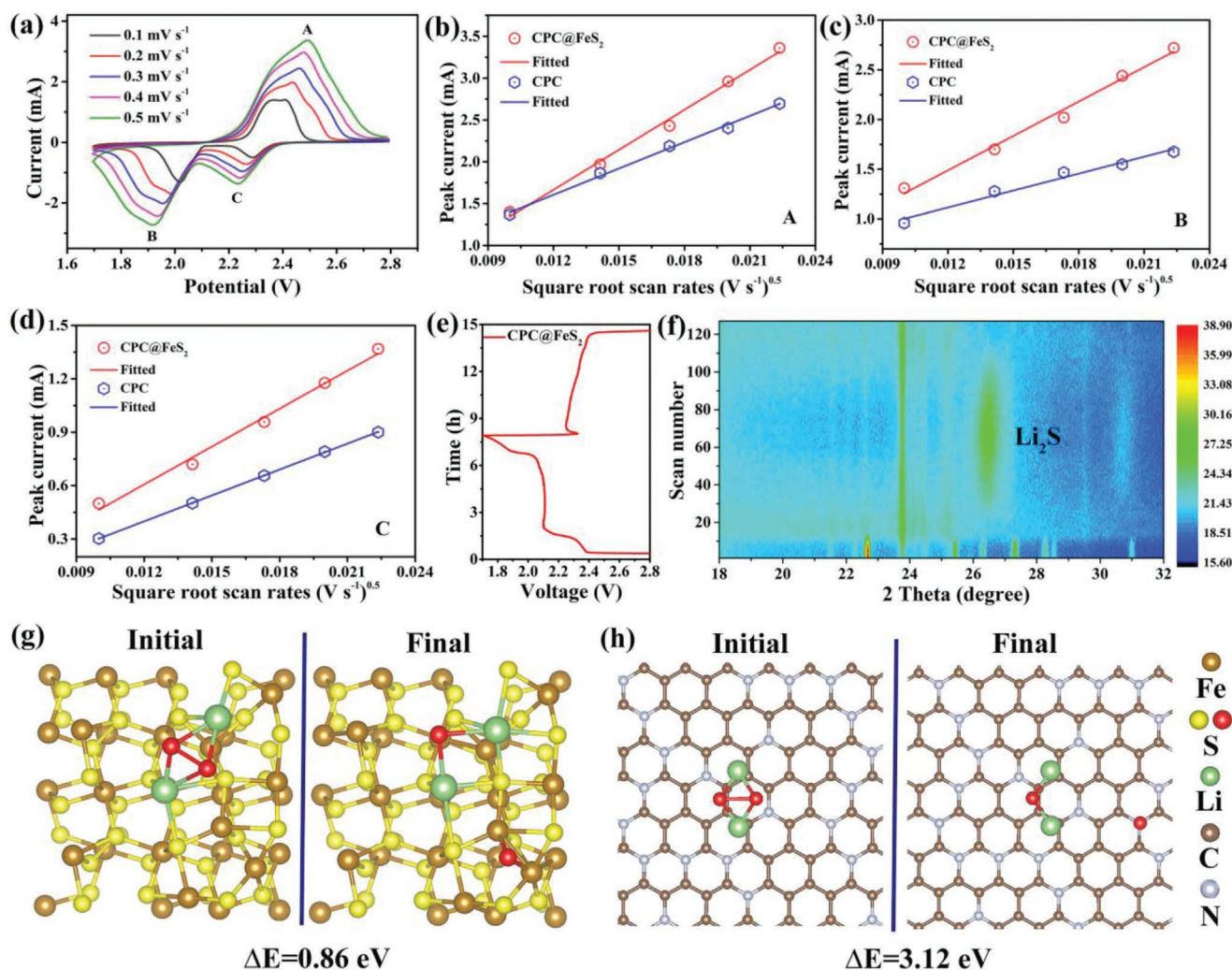


**Figure 5.** Electrochemical kinetic of sulfur species on CPC@FeS<sub>2</sub> host. a) CV curves of S/CPC@FeS<sub>2</sub> cathode under different scanning rates from 0.1 to 0.5 mV s<sup>-1</sup>. b–d) Peak current for the cathodic and anodic peaks A, B, and C for S/CPC@FeS<sub>2</sub> and S/CPC cathodes versus the square root of scanning rate. e, f) In situ XRD contour plots (f) of S/CPC@FeS<sub>2</sub> cathode and the corresponding discharge/charge curve (e). g, h) Dissociation energy (ΔE) of Li<sub>2</sub>S<sub>2</sub> to form Li<sub>2</sub>S on the surface of FeS<sub>2</sub> (g) and N-doped carbon (h).

battery, which is including the adsorption of LiPSs to the surface of carbon host, diffusion of Li-ion and the dissociation from Li<sub>2</sub>S<sub>2</sub> to Li<sub>2</sub>S, as shown in Figure S9 of the Supporting Information. To investigate the role of Li-ion diffusivity on the kinetic of conversion reaction for sulfur species, cyclic voltammetry (CV) under various scanning rates (0.1–0.5 mV s<sup>-1</sup>) were carried out for S/CPC@FeS<sub>2</sub> cathode and S/CPC cathode, which is prepared with CPC host. The correlation between peak currents for anodic and cathodic reactions (Figure 5a; Figure S10, Supporting Information) with the square root of scanning rates is described by the Randles–Sevcik equation<sup>[42]</sup>

$$I_p = 2.69 \times 10^5 \cdot n^{1.5} \cdot S \cdot D_{Li^+}^{0.5} \cdot C_{Li^+} \cdot \nu^{0.5} \quad (1)$$

where  $I_p$  is the value of peak current,  $n$  is the number of transferred electrons for the reaction,  $S$  is the area of electrode,  $D_{Li^+}$  is the diffusion coefficient for Li<sup>+</sup>,  $C_{Li^+}$  is the concentration of Li<sup>+</sup> in electrolyte, and  $\nu$  represents the scanning rate. Therefore,

the slope of  $I_p/\nu^{0.5}$  is used to estimate the diffusion coefficient of Li<sup>+</sup>. The fitted slopes for the three reactions in Figure 5b–d shows that the value for S/CPC@FeS<sub>2</sub> cathode are greater than that for S/CPC cathode, indicating higher diffusion coefficients of Li<sup>+</sup> in the S/CPC@FeS<sub>2</sub> cathode, which is beneficial to the conversion reaction kinetics of sulfur species.

For the conversion reactions in Li–S battery, the solid–solid transformation between Li<sub>2</sub>S<sub>2</sub> and Li<sub>2</sub>S is considered the main rate controlling step and this process contributes half the theoretical capacity.<sup>[31]</sup> Here, in situ XRD was conducted to track the catalytic conversion process of Li<sub>2</sub>S on the CPC@FeS<sub>2</sub> host. The in situ cell made of S/CPC@FeS<sub>2</sub> cathode was cycling at a rate of 0.1 C and the XRD patterns in a contour plot as well as corresponding voltage profile are shown in Figure 5e, f and Figure S11 (Supporting Information). During the discharge process, the characteristic peaks for sulfur are obviously detected at the initial stage and its intensity gradually reduces with the increasing depth of discharge. At the same time, the



characteristic peak for  $\text{Li}_2\text{S}$  at  $\approx 26.5^\circ$  shows up.<sup>[17]</sup> At the end of discharge process, the peaks for sulfur disappear while the highest intensity of the peak for  $\text{Li}_2\text{S}$  is obtained, indicating an efficient conversion of sulfur species to  $\text{Li}_2\text{S}$  on the CPC@ $\text{FeS}_2$  host. During the charge process, the intensity of the peak for  $\text{Li}_2\text{S}$  shows a gradual reduction, suggesting a high reversibility for the conversion of  $\text{Li}_2\text{S}$  to  $\text{Li}_2\text{S}_2$  or polysulfides in the S/CPC@ $\text{FeS}_2$  cathode. The catalytic mechanism of  $\text{FeS}_2$  for the conversion from  $\text{Li}_2\text{S}_2$  to  $\text{Li}_2\text{S}$  is further demonstrated by the DFT calculations. The optimized atomic structure of  $\text{Li}_2\text{S}_2$  is simulated for its adsorption on surface of the  $\text{FeS}_2$  and N-doped carbon, see Figure 5g,h. The binding energy for  $\text{FeS}_2$  and  $\text{Li}_2\text{S}_2$  is 4.38 and it is 0.61 eV for the adsorption of  $\text{Li}_2\text{S}_2$  on N-doped carbon surface, revealing a good chemical affinity of  $\text{Li}_2\text{S}_2$  to  $\text{FeS}_2$ . Moreover, the dissociation energy ( $\Delta E$ ) of  $\text{Li}_2\text{S}_2$  on  $\text{FeS}_2$  surface is calculated as 0.86 eV, which is much smaller than that on the surface of N-doped carbon (3.12 eV). This suggests that the energy barrier for the conversion from  $\text{Li}_2\text{S}_2$  to  $\text{Li}_2\text{S}$  on the surface of  $\text{FeS}_2$  is significantly lowered and the efficient catalytic activity of  $\text{FeS}_2$  will promote the utilization of active mass for Li-S battery.

The catalytic activity of the CPC@ $\text{FeS}_2$  host is further examined in Li-S cells by CV and electrochemical impedance spectroscopy (EIS). The CV profiles (Figure 6a) of S/CPC@ $\text{FeS}_2$  and

S/CPC cathodes shows two typical cathodic peaks which are corresponding to reduction of sulfur to LiPSs and the following reduction to  $\text{Li}_2\text{S}_2/\text{Li}_2\text{S}$ , and one anodic peak, which is assigned to the reverse oxidation reactions.<sup>[52]</sup> The smaller potential difference for the anodic peak and the second cathodic peak and higher peak current indicates that the conversion reaction kinetics for S/CPC@ $\text{FeS}_2$  cathode is accelerated compared with that in S/CPC cathode.<sup>[53]</sup> The CV profile of pure CPC@ $\text{FeS}_2$  is also obtained with the range from 1.7 to 2.8 V, which is shown in Figure S12 of the Supporting Information. It can be seen that no redox reactions of CPC@ $\text{FeS}_2$  exist under this conditions. The EIS spectra (Figure 6b) show that the diameter of semi-circle corresponding to the charge transfer resistance is smaller for S/CPC@ $\text{FeS}_2$  cathode, revealing a faster charge transfer in this cathode. The voltage profiles (Figure 6c) for various sulfur cathodes in coin cells show the impact of  $\text{FeS}_2$  electrocatalyst on the charge/discharge process of Li-S battery. For the charge process, a lower potential of 1.87 V at initial stage and a smaller potential barrier of 2.24 V are obtained in S/CPC@ $\text{FeS}_2$  cathode, suggesting that there are more reductive sulfur species produced in the cathode and the conversion kinetic for  $\text{Li}_2\text{S}$  is boosted.<sup>[17]</sup> Moreover, the lower polarization between charge and discharge further demonstrates the function of CPC@ $\text{FeS}_2$  host as effective electrocatalyst.

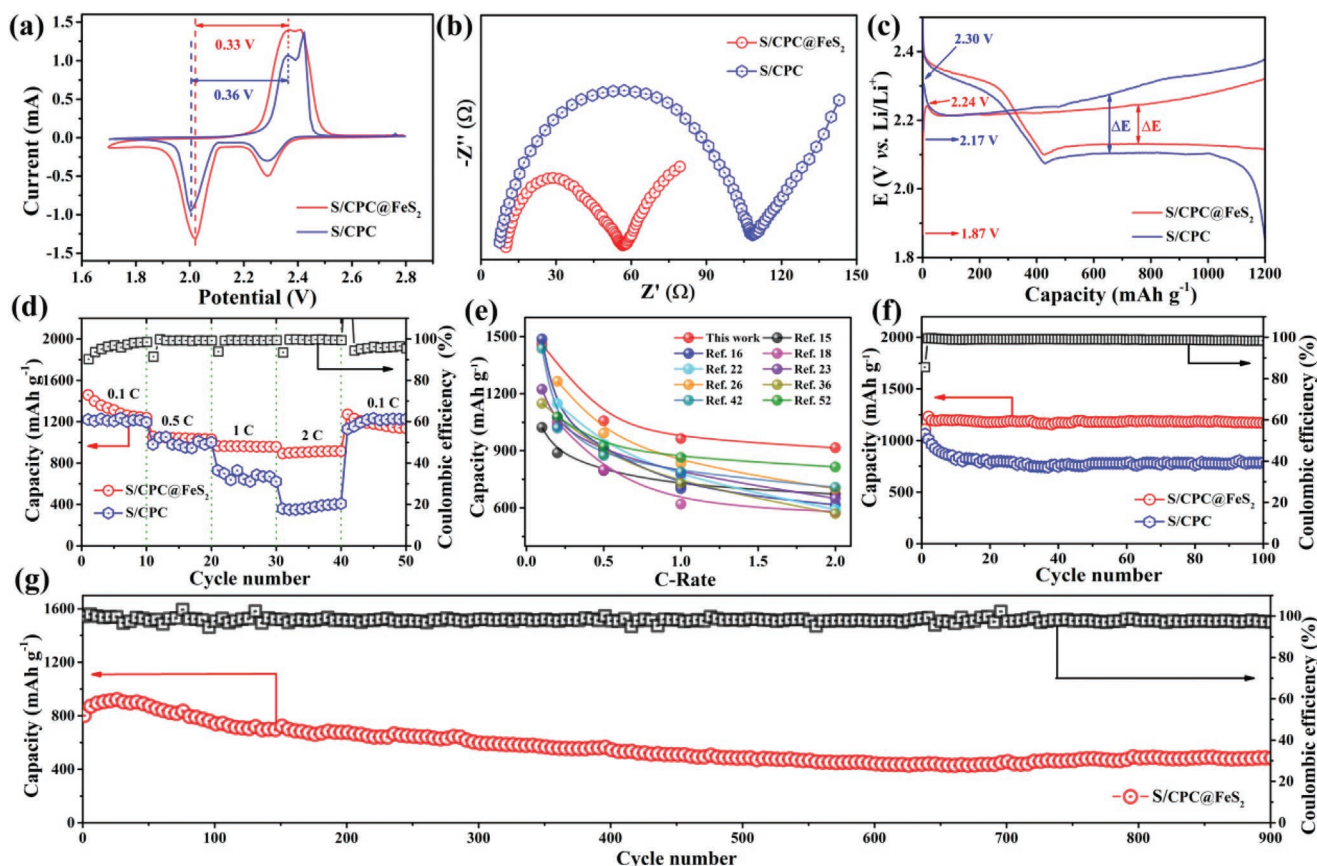


**Figure 6.** Electrochemical performance of Li-S coin cells. a) Comparison of potential difference from CV profiles at 0.1 mV s<sup>-1</sup>. b) EIS plots of different cathodes before cycling. c,d) voltage profile at 0.1 C (c) and rate capabilities (d) of Li-S cells using S/CPC@ $\text{FeS}_2$  and S/CPC cathodes. e) Comparisons of rate performance between this work with reported prevailing sulfur hosts. f) Cycling performance of Li-S cells at 0.4 C with S/CPC@ $\text{FeS}_2$  and S/CPC cathodes. g) Cycling stability and Coulombic efficiency of S/CPC@ $\text{FeS}_2$  cathode at 1.5 C.



The electrochemical performance of S/CPC@FeS<sub>2</sub> cathode is evaluated by galvanostatic cycling under various rates within a voltage range of 1.7–2.8 V, as shown in Figure 6d. The S/CPC@FeS<sub>2</sub> cathode shows a highest capacity of 1459 mAh g<sup>-1</sup> at 0.1 C and a capacity of 916 mAh g<sup>-1</sup> under high rate of 2 C, which are outstanding among the results reported for host materials in sulfur cathodes (Figure 6e). By contrast, the S/CPC cathode without FeS<sub>2</sub> electrocatalyst only shows a capacity of 407 mAh g<sup>-1</sup> at 2 C. The cycling performance of S/CPC@FeS<sub>2</sub> and S/CPC cathodes is examined at 0.4 C for 100 cycles, see Figure 6f. The specific capacity for S/CPC@FeS<sub>2</sub> cathode is 1232 mAh g<sup>-1</sup> at initial cycles and it maintains 1171 mAh g<sup>-1</sup> after cycling, showing 95% of the capacity retention with a high Coulombic efficiency of 99% during the whole cycling. However, the S/CPC cathode only maintains 74% of the initial capacity. To demonstrate the cycling stability of S/CPC@FeS<sub>2</sub>

cathode under practical conditions, a long-term cycling of S/CPC@FeS<sub>2</sub> cathode is performed under 1.5 C for 900 cycles, as seen in Figure 6g. A capacity retention of 60% is obtained and the fading rate for each cycle is as low as 0.043%, showing a competitive cycling performance compared with previous reports of sulfur cathodes listed in Table S1 of the Supporting Information.

To demonstrate the capability of large-scale preparation of this host material and its application, S/CPC@FeS<sub>2</sub> cathode is used to assemble Li–S pouch cells (Figure 7a). The Li–S pouch cell is made of S/CPC@FeS<sub>2</sub> cathode, Li foil as well as Celgard separator, and it is assembled by coiling procedure and finally packed into a laminate bag. To achieve high energy density for the cell, a high sulfur loading ( $\geq 7$  mg cm<sup>-2</sup>) in S/CPC@FeS<sub>2</sub> cathode and a lean electrolyte (E/S ratio  $\leq 4$   $\mu$ L mg<sup>-1</sup>) are applied. The Li–S pouch cell is tested at 0.1 C and the voltage profiles

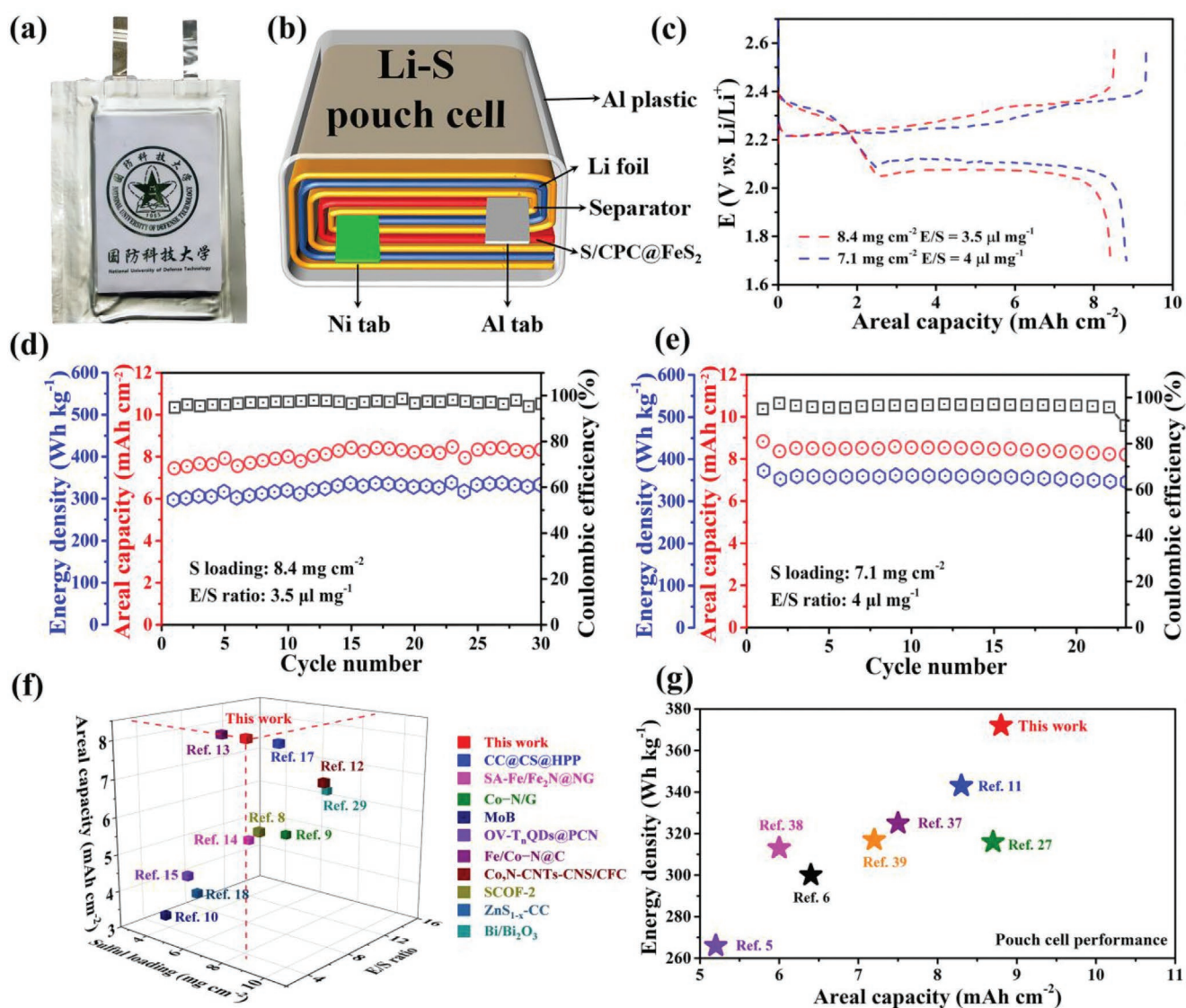


**Figure 7.** Electrochemical performance of Li–S pouch cells with high loading S/CPC@FeS<sub>2</sub> cathode. a) Photograph and b) schematic diagram of Li–S pouch cells. c) Discharge–charge profiles of Li–S pouch cell with different sulfur loading and E/S ratio at 0.1 C. d,e) Cycling stability of Li–S pouch cells at 0.1 C. f) Comparison of key parameters (E/S ratio, sulfur loading, and areal capacity) of pouch cells in this work with reported data. g) Comparison of areal density and energy density with previously reported Li–S pouch cells.

are displayed in Figure 7c, showing two typical plateaus for discharge process as in coin cells. As shown in Figure 7d, the pouch cell delivers a high areal capacity is  $8.5 \text{ mAh cm}^{-2}$  from the sulfur loading of  $8.4 \text{ mg cm}^{-2}$  in the cathode under an ultralow E/S ratio of  $3.5 \text{ }\mu\text{L mg}^{-1}$  and this gives a capacity of  $1008 \text{ mAh g}^{-1}$  for active mass and a high energy density of  $338 \text{ Wh kg}^{-1}$  at cell level including entire weight of sulfur cathode, current collector, electrolyte, separator, and Li anode. Moreover, this pouch cell shows a retention energy density of  $333 \text{ Wh kg}^{-1}$  after 30 cycles. To achieve higher energy density for Li–S pouch cell, the sulfur loading and E/S ratio are furthered optimized to obtain a high specific capacity of  $1239 \text{ mAh g}^{-1}$  for active mass, which is a significant improvement in pouch cells. The cell with lower sulfur loading of  $7.1 \text{ mg cm}^{-2}$  and higher E/S ratio of  $4 \text{ }\mu\text{L mg}^{-1}$  delivers a similar areal capacity of  $8.8 \text{ mAh cm}^{-2}$  and much higher energy density of  $372 \text{ Wh kg}^{-1}$ , see Figure 7e. This suggests that specific capacity for active mass is another important aspect to be considered for high energy density Li–S battery besides the sulfur loading and E/S ratio. By contrast, the Li–S cell using S/CPC cathode only has a specific capacity of  $958 \text{ mAh g}^{-1}$  and energy density of  $288 \text{ Wh kg}^{-1}$  under similar conditions (sulfur loading of  $7.2 \text{ mg cm}^{-2}$  and E/S ratio of  $4 \text{ }\mu\text{L mg}^{-1}$ , Figure S13, Supporting Information). The advanced performance of Li–S cell with S/CPC@FeS<sub>2</sub> cathode is also compared with previous reports and shows a great achievement (Figure 7f,g). To show the potential application of Li–S pouch cell, an array of light-emitting diodes with a pattern is powered by a cell, see Figure S14 of the Supporting Information.

### 3. Conclusions

In this work, we designed and synthesized a CPC@FeS<sub>2</sub> host in which the nitrogen-doped continuous porous carbon is anchored with the catalytic FeS<sub>2</sub> nanoclusters, and this host shows a great promise to build high performance sulfur cathode for Li–S battery. The CPC@FeS<sub>2</sub> host has a highly conductive network for electrons, a robust porous architecture, and active sites of electrocatalyst, providing a multifunctional carrier for the conversion of sulfur species. The host material shows a strong adsorption to LiPSs, enhanced diffusivity of Li-ion and the accelerated kinetics for the sluggish solid–solid transformation of Li<sub>2</sub>S<sub>2</sub> to Li<sub>2</sub>S, which are beneficial to high utilization of active mass and rate capability of sulfur cathode. Therefore, the S/CPC@FeS<sub>2</sub> sulfur cathode delivers a high specific capacity of  $1459 \text{ mAh g}^{-1}$  and a stable cycling over 900 cycles. The Li–S pouch cell with this sulfur cathode has a high energy density  $372 \text{ Wh kg}^{-1}$  under practical conditions with a sulfur loading of  $7.1 \text{ mg cm}^{-2}$  and an E/S ratio of  $4 \text{ }\mu\text{L mg}^{-1}$ . Our work not only provides a strategy to design carbon host material for efficient conversion of sulfur species, but also shows the capability for large-scale application of this material in high energy Li–S battery.

### 4. Experimental Section

**Synthesis of CPC@FeS<sub>2</sub> Host:** Nitrogen-doped CPC was synthesized by the modified procedure reported in previous literature.<sup>[40]</sup> Briefly,

1 g melamine and 10 g sodium citrate were mixed through grinding in a mortar and subsequently the mixture was annealed at  $700 \text{ }^{\circ}\text{C}$  for 2 h under argon atmosphere. The product after annealing was dispersed in a solution of 4 M HCl and stirred for 24 h. The CPC was obtained after filtrating and drying at  $80 \text{ }^{\circ}\text{C}$  for 12 h. To prepare CPC@FeS<sub>2</sub> host, 0.2 g CPC powder was dispersed in 50 mL of 0.1 M FeCl<sub>3</sub> solution and subsequently stirred at  $45 \text{ }^{\circ}\text{C}$  for 6 h to obtain fully adsorption of Fe<sup>3+</sup>. The product was collected by filtering and drying, then mixed with sublimed sulfur and calcined at  $350 \text{ }^{\circ}\text{C}$  for 3 h under argon atmosphere.

**Synthesis of S/CPC and S/CPC@FeS<sub>2</sub> Composite:** Both S/CPC and S/CPC@FeS<sub>2</sub> composites were prepared by the classical melting diffusion method. The host material (CPC or CPC@FeS<sub>2</sub>) was mixed with sulfur by a weight ratio of 1:5 in 10 mL of CS<sub>2</sub> and then stirred for 5 h to evaporate the solvent. The mixture was further heated at  $155 \text{ }^{\circ}\text{C}$  for 12 h to obtain the cathode material.

**Characterization:** XRD measurements for identifying crystalline structure and composition of the materials were conducted on Rigaku TTR-3 system with a Cu K $\alpha$  radiation. Morphology of the carbon samples was obtained by SEM (Hitachi S-4800). TEM analysis was performed with a Tecnai F20 TEM system equipped with the EDS. Zeta potential of CPC powder was measured by a zeta sizer system (Malvern Instruments). The chemical analysis of sample surface was conducted on a PHI-1600 X-ray photoelectron spectroscopy (XPS). TGA (TGA-600) of samples was performed at a heating rate of  $10 \text{ }^{\circ}\text{C min}^{-1}$  in argon atmosphere. The distribution of pores and specific surface area of CPC host were measured by BET method. In situ XRD measurement on Li–S cell was performed on a Bruker X-ray diffractometer and the cell was operated between 1.7 and 2.8 V at a rate of 0.1 C rate.

**Adsorption Measurement for LiPSs:** The solution of Li<sub>2</sub>S<sub>6</sub> was prepared by mixing sulfur and Li<sub>2</sub>S with a molar ratio of 1:5 in the mixed solvent (1,3-dioxolane and 1,2-dimethoxyethane, v/v = 1:1) for 12 h stirring. Next, 5 mg of CPC or CPC@FeS<sub>2</sub> powder was added into the Li<sub>2</sub>S<sub>6</sub> solution for fully adsorption of LiPSs and the CPC@FeS<sub>2</sub>/Li<sub>2</sub>S<sub>6</sub> powder was obtained after filtrating and drying for XPS measurement.

**Electrochemical Tests:** The electrochemical performance of the S/CPC and S/CPC@FeS<sub>2</sub> cathodes was first evaluated in standard CR2032 coin cell. The coin cell was assembled with sulfur cathode, electrolyte (1 M lithium bis(trifluoromethanesulfonyl)imide and 0.2 M lithium nitrate in the mixed solvent of 1,3-dioxolane and 1,2-dimethoxymethane with volume ratio of 1:1), and Li foil in an argon atmosphere glovebox. The average loading of sulfur in cathodes for coin cells was  $\approx 1.6 \text{ mg cm}^{-2}$ , and the E/S ratio was set as  $15 \text{ }\mu\text{L mg}^{-1}$ . The discharge/charge cycling of coin cells was performed on LAND system under the range of 1.7 and 2.8 V. The currents for rate capability were calculated with  $1 \text{ C} = 1675 \text{ mA g}^{-1}$ . The CV and EIS measurements were conducted on a Princeton VersaSTAT potentiostat system. For fabrication of pouch cell, the sulfur cathode was prepared by dispersing S/CPC@FeS<sub>2</sub> composite, Super P and LA133 binder in deionized water with a mass fraction of 87:7:6. Subsequently, the slurry was casted on Al foil and dried under vacuum at  $60 \text{ }^{\circ}\text{C}$  for 12 h. The pouch cell was assembled by coiling sulfur cathode, Celgard 2400, and lithium foil with a sandwich structure. High sulfur loading and low E/S ratio was applied for pouch cells, see Section 2.

**Calculation of Energy Density for Pouch Cell:** The energy density of Li–S pouch cell ( $E_{\text{cell}}$ ) was estimated at device level by the equation

$$E_{\text{cell}} = CV / M = M_s C_s V / (M_{\text{Al}} + M_{\text{cat}} + M_{\text{ele}} + M_{\text{Li}} + M_{\text{sep}}) \quad (2)$$

where  $C$  is the capacity (mAh),  $V$  is the average voltage of cell (V),  $M_s$  is the areal loading of sulfur in cathode ( $\text{mg cm}^{-2}$ ),  $C_s$  is the specific capacity of active mass ( $\text{mAh g}^{-1}$ ),  $M_{\text{Al}}$  is the areal mass of Al foil ( $\text{mg cm}^{-2}$ ),  $M_{\text{cat}}$  is the areal mass of the whole cathode ( $\text{mg cm}^{-2}$ ),  $M_{\text{ele}}$  is the areal mass of electrolyte ( $\text{mg cm}^{-2}$ ),  $M_{\text{Li}}$  is the areal mass of Li foil ( $\text{mg cm}^{-2}$ ), and  $M_{\text{sep}}$  is the areal mass of separator ( $\text{mg cm}^{-2}$ ).

**Theoretical Calculations:** DFT computation in this work was carried out using the Vienna ab initio simulation package. Projector augmented wave potentials<sup>[46–48]</sup> and Perdew–Burke–Ernzerhof functional within the generalized gradient approximation<sup>[49]</sup> were employed in the simulation.



The  $2 \times 2$  supercell for  $\text{FeS}_2$  (200) surfaces was built. The vacuum space along the  $z$  direction was set as  $15 \text{ \AA}$  while the cutoff energy was set as  $500 \text{ eV}$ . The Brillouin zone of the supercell was sampled by a  $3 \times 3 \times 1$   $k$ -point sampling grid and the convergence tolerances of energy and force was set  $1.0 \times 10^{-4} \text{ eV per atom}$  and  $10^{-2} \text{ eV \AA}^{-1}$ , respectively. The DFT-D3 method was used to describe van der Waals interaction.<sup>[50]</sup> Spin polarization was included to describe the magnetic properties. The structure for  $\text{Li}_2\text{S}_2$  was adequately optimized in a  $15 \text{ \AA} \times 15 \text{ \AA} \times 15 \text{ \AA}$  vacuum unit cell. The binding energy ( $E_b$ ) of LiPSs on  $\text{FeS}_2$  (200) surfaces was calculated by following equation

$$E_b = E_{\text{sub+LiPS}} - E_{\text{LiPS}} - E_{\text{sub}} \quad (3)$$

where  $E_{\text{sub+LiPS}}$  is the total energy of the  $\text{FeS}_2$  surface with adsorbed LiPS,  $E_{\text{LiPS}}$  is the total energy of certain LiPS, and  $E_{\text{sub}}$  is the total energy of  $\text{FeS}_2$ .

## Supporting Information

Supporting Information is available from the Wiley Online Library or from the author.

## Acknowledgements

W.S. and S.L. contributed equally to this work. The authors acknowledge the financial support from the Natural Science Foundation of Hunan Province (Nos. 2022JJ40551 and 2022JJ30663), National University of Defense Technology (Grant No. ZK19-27), and Significant Independent Research Projects for Young Talents of College of Aerospace Science and Engineering, National University of Defense Technology.

## Conflict of Interest

The authors declare no conflict of interest.

## Data Availability Statement

The data that support the findings of this study are available from the corresponding author upon reasonable request.

## Keywords

electrocatalyses, high energy densities, high sulfur loading, lithium–sulfur batteries, pouch cells

Received: May 13, 2022

Revised: July 27, 2022

Published online:

- [1] F. Wu, J. Maier, Y. Yu, *Chem. Soc. Rev.* **2020**, 49, 1569.
- [2] Z. P. Cano, D. Banham, S. Ye, A. Hintennach, J. Lu, M. Fowler, Z. Chen, *Nat. Energy* **2018**, 3, 279.
- [3] P. Yan, J. Zheng, J. Liu, B. Wang, X. Cheng, Y. Zhang, X. Sun, C. Wang, J.-G. Zhang, *Nat. Energy* **2018**, 3, 600.
- [4] W. Sun, Y. Li, K. Xie, S. Luo, G. Bai, X. Tan, C. Zheng, *Nano Energy* **2018**, 54, 175.
- [5] H. Li, Y. Tao, C. Zhang, D. Liu, J. Luo, W. Fan, Y. Xu, Y. Li, C. You, Z. Z. Pan, *Adv. Energy Mater.* **2018**, 8, 1703438.

- [6] M. Zhao, B.-Q. Li, X. Chen, J. Xie, H. Yuan, J.-Q. Huang, *Chem* **2020**, 6, 3297.
- [7] W. Deng, J. Phung, G. Li, X. Wang, *Nano Energy* **2021**, 82, 105761.
- [8] J. Xu, S. An, X. Song, Y. Cao, N. Wang, X. Qiu, Y. Zhang, J. Chen, X. Duan, J. Huang, *Adv. Mater.* **2021**, 33, 2105178.
- [9] Z. Du, X. Chen, W. Hu, C. Chuang, S. Xie, A. Hu, W. Yan, X. Kong, X. Wu, H. Ji, *J. Am. Chem. Soc.* **2019**, 141, 3977.
- [10] J. He, A. Bhargava, A. Manthiram, *Adv. Mater.* **2020**, 32, 2004741.
- [11] C.-X. Zhao, X.-Y. Li, M. Zhao, Z.-X. Chen, Y.-W. Song, W.-J. Chen, J.-N. Liu, B. Wang, X.-Q. Zhang, C.-M. Chen, *J. Am. Chem. Soc.* **2021**, 143, 19865.
- [12] D. Fang, Y. Wang, C. Qian, X. Liu, X. Wang, S. Chen, S. Zhang, *Adv. Funct. Mater.* **2019**, 29, 1900875.
- [13] H. Ye, J. Sun, S. Zhang, H. Lin, T. Zhang, Q. Yao, J. Y. Lee, *ACS Nano* **2019**, 13, 14208.
- [14] C. Ma, Y. Zhang, Y. Feng, N. Wang, L. Zhou, C. Liang, L. Chen, Y. Lai, X. Ji, C. Yan, *Adv. Mater.* **2021**, 33, 2100171.
- [15] H. Zhang, L. Yang, P. Zhang, C. Lu, D. Sha, B. Yan, W. He, M. Zhou, W. Zhang, L. Pan, *Adv. Mater.* **2021**, 33, 2008447.
- [16] B. Jiang, Y. Qiu, D. Tian, Y. Zhang, X. Song, C. Zhao, M. Wang, X. Sun, H. Huang, C. Zhao, *Adv. Energy Mater.* **2021**, 11, 2102995.
- [17] Z. Ye, Y. Jiang, L. Li, F. Wu, R. Chen, *Adv. Mater.* **2020**, 32, 2002168.
- [18] J. Wang, Y. Zhao, G. Li, D. Luo, J. Liu, Y. Zhang, X. Wang, L. Shui, Z. Chen, *Nano Energy* **2021**, 84, 105891.
- [19] J. Liu, S. H. Xiao, Z. Zhang, Y. Chen, Y. Xiang, X. Liu, J. S. Chen, P. Chen, *Nanoscale* **2020**, 12, 5114.
- [20] J. Liu, S. Xiao, X. Liu, R. Wu, X. Niu, Y. Xiang, J. S. Chen, C. Yang, *Chem. Eng. J.* **2021**, 423, 130246.
- [21] W. Sun, C. Liu, Y. Li, S. Luo, S. Liu, X. Hong, K. Xie, Y. Liu, X. Tan, C. Zheng, *ACS Nano* **2019**, 13, 12137.
- [22] Y. Wang, R. Zhang, Y.-c. Pang, X. Chen, J. Lang, J. Xu, C. Xiao, H. Li, K. Xi, S. Ding, *Energy Storage Mater.* **2019**, 16, 228.
- [23] Z. Shen, M. Cao, Z. Zhang, J. Pu, C. Zhong, J. Li, H. Ma, F. Li, J. Zhu, F. Pan, *Adv. Funct. Mater.* **2020**, 30, 1906661.
- [24] X. Chen, S. Zeng, H. Muheiyati, Y. Zhai, C. Li, X. Ding, L. Wang, D. Wang, L. Xu, Y. He, *ACS Energy Lett.* **2019**, 4, 1496.
- [25] J. Shen, X. Xu, J. Liu, Z. Wang, S. Zuo, Z. Liu, D. Zhang, J. Liu, M. Zhu, *Adv. Energy Mater.* **2021**, 11, 2100673.
- [26] Y. Zhang, G. Li, J. Wang, G. Cui, X. Wei, L. Shui, K. Kempa, G. Zhou, X. Wang, Z. Chen, *Adv. Funct. Mater.* **2020**, 30, 2001165.
- [27] F. Wu, Y.-S. Ye, J.-Q. Huang, T. Zhao, J. Qian, Y.-Y. Zhao, L. Li, L. Wei, R. Luo, Y.-X. Huang, *ACS Nano* **2017**, 11, 4694.
- [28] Z. Liang, J. Shen, X. Xu, F. Li, J. Liu, B. Yuan, Y. Yu, M. Zhu, *Adv. Mater.* **2022**, 34, 2200102.
- [29] Y. Xiao, S. Guo, Y. Ouyang, D. Li, X. Li, W. He, H. Deng, W. Gong, C. Tan, Q. Zeng, *ACS Nano* **2021**, 15, 18363.
- [30] Z. Jin, T. Lin, H. Jia, B. Liu, Q. Zhang, L. Li, L. Zhang, Z.-M. Su, C. Wang, *ACS Nano* **2021**, 15, 7318.
- [31] X. Yang, X. Gao, Q. Sun, S. P. Jand, Y. Yu, Y. Zhao, X. Li, K. Adair, L. Y. Kuo, J. Rohrer, *Adv. Mater.* **2019**, 31, 1901220.
- [32] J.-L. Yang, D.-Q. Cai, Q. Lin, X.-Y. Wang, Z.-Q. Fang, L. Huang, Z.-J. Wang, X.-G. Hao, S.-X. Zhao, J. Li, *Nano Energy* **2021**, 91, 106669.
- [33] D. Zheng, Z. Jing, Q. Zhao, Y. Kim, P. Li, H. Xu, Z. Li, J. Lin, *Chem. Eng. J.* **2020**, 402, 125069.
- [34] Y. Cao, S. Huang, Z. Peng, F. Yao, X. Li, Y. Liu, H. Huang, M. Wu, *J. Mater. Chem. A* **2021**, 9, 3464.
- [35] K. Xi, D. He, C. Harris, Y. Wang, C. Lai, H. Li, P. R. Coxon, S. Ding, C. Wang, R. V. Kumar, *Adv. Sci.* **2019**, 6, 1800815.
- [36] R. Li, H. Shen, E. Pervaiz, M. Yang, *Chem. Eng. J.* **2021**, 404, 126462.
- [37] Y. Liu, Y. Barnscheidt, M. Peng, F. Bettels, T. Li, T. He, F. Ding, L. Zhang, *Adv. Sci.* **2021**, 8, 2101182.

- [38] L. Shi, S.-M. Bak, Z. Shadike, C. Wang, C. Niu, P. Northrup, H. Lee, A. Y. Baranovskiy, C. S. Anderson, J. Qin, *Energy Environ. Sci.* **2020**, 13, 3620.
- [39] C. Zhao, G.-L. Xu, Z. Yu, L. Zhang, I. Hwang, Y.-X. Mo, Y. Ren, L. Cheng, C.-J. Sun, Y. Ren, *Nat. Nanotechnol.* **2021**, 16, 166.
- [40] W. Yang, W. Yang, F. Ding, L. Sang, Z. Ma, G. Shao, *Carbon* **2017**, 111, 419.
- [41] C. Zhou, X. Li, H. Jiang, Y. Ding, G. He, J. Guo, Z. Chu, G. Yu, *Adv. Funct. Mater.* **2021**, 31, 2011249.
- [42] D. Cai, B. Liu, D. Zhu, D. Chen, M. Lu, J. Cao, Y. Wang, W. Huang, Y. Shao, H. Tu, *Adv. Energy Mater.* **2020**, 10, 1904273.
- [43] Z. Man, P. Li, D. Zhou, Y. Wang, X. Liang, R. Zang, P. Li, Y. Zuo, Y. M. Lam, G. Wang, *Nano Lett.* **2020**, 20, 3769.
- [44] Z. Qiao, Y. Zhang, Z. Meng, Q. Xie, L. Lin, H. Zheng, B. Sa, J. Lin, L. Wang, D. L. Peng, *Adv. Funct. Mater.* **2021**, 31, 2100970.
- [45] B. Liu, S. Huang, D. Kong, J. Hu, H. Y. Yang, *J. Mater. Chem. A* **2019**, 7, 7604.
- [46] G. Kresse, D. Joubert, *Phys. Rev. B* **1999**, 59, 1758.
- [47] G. Kresse, J. Furthmüller, *Comp. Mater. Sci.* **1996**, 6, 15.
- [48] G. Kresse, J. Furthmüller, *Phys. Rev. B* **1996**, 54, 11169.
- [49] J. P. Perdew, K. Burke, M. Ernzerhof, *Phys. Rev. Lett.* **1996**, 77, 3865.
- [50] K. Lee, É. D. Murray, L. Kong, B. I. Lundqvist, D. C. Langreth, *Phys. Rev. B* **2010**, 82, 081101.
- [51] Z. Li, Q. He, X. Xu, Y. Zhao, X. Liu, C. Zhou, D. Ai, L. Xia, L. Mai, *Adv. Mater.* **2018**, 30, 1804089.
- [52] H. Zhang, L. K. Ono, G. Tong, Y. Liu, Y. Qi, *Nat. Commun.* **2021**, 12, 4738.
- [53] S. Wang, S. Feng, J. Liang, Q. Su, F. Zhao, H. Song, M. Zheng, Q. Sun, Z. Song, X. Jia, *Adv. Energy Mater.* **2021**, 11, 2003314.